

Estimating fMRI Timescale Maps

Abstract

Timescales describe the rate at which time-dependent processes decay, encompassing the activity of individual neurons, neural populations, and large-scale brain networks. The spatial organization of timescales across brain regions offers mechanistic insights into how these regions integrate and process information over time. Despite their functional significance, current methods for estimating timescales often rely on restrictive assumptions and report only point estimates, limiting statistical inference and comparisons across individual brains or experimental conditions. This paper introduces two robust models for timescale estimation, a time-domain linear model and an autocorrelation-domain nonlinear model, both evaluated under general assumptions. We establish the theoretical properties of these models (bias, consistency, and limiting variance) enabling the assignment of standard errors to point estimates, which facilitates hypothesis testing and the construction of confidence intervals. Sampling bias and variance are also evaluated through simulations and timescale maps are estimated using resting fMRI from the Human Connectome Project. Comparatively, the linear model is more computationally efficient and scalable to mass-univariate settings like fMRI, while the nonlinear model is more sensitive to long-range temporal dependencies. Both models employ robust standard errors to address biases under model misspecification, improving reliability in both simulated and empirical settings. Taken together, these methods yield cortical timescale maps consistent with known anatomical hierarchies, enhancing our understanding of neural dynamics. This work provides a robust framework for mapping and inferring neural timescales, facilitating more reliable comparisons across brain regions, experimental conditions, and individuals.

1 Introduction

1.1 Scientific Motivation

Brain activity spans a range of timescales, from the rapid dynamics of synaptic events to the slower oscillatory activities that coordinate neuron populations and large-scale networks [2]. These timescales are spatially organized and align with anatomical maps, progressively increasing from sensory to associative brain regions [29, 6, 10]. Multimodal evidence suggests that these timescales arise from intrinsic properties of brain anatomy and reveal how different regions integrate and process information over time.

Timescale maps align with the well-established functional hierarchy in the brain, where sensory areas, which process rapidly changing stimuli, exhibit faster timescales than higher-order association areas involved in complex cognitive processes that unfold over longer durations [25, 10, 37]. The emergence of hierarchical timescales likely depends on multiple mechanisms. Computational modeling by Li and Wang [16] suggest three key factors: 1) a brain-wide gradient in the strength of synaptic excitation, 2) differences in the electrophysiological properties of excitatory versus inhibitory neurons, and 3) the balance between excitatory inputs from distant brain regions and inhibitory inputs from local

circuits.

Further, timescales are not static but can be dynamically modulated by experimental manipulations or behavioral demands. Pharmacological agents, such as propofol and serotonergic drugs, can alter intrinsic timescales, affecting the temporal integration of information in the brain [13, 35]. Further, research has shown changes in timescales across sleep deprivation and wakefulness, neuropsychiatric disorders like autism and schizophrenia, as well as naturalistic behaviors [22, 40, 41, 21]. Taken together, these findings demonstrate that timescales have broad relevance to both structural and functional properties of the brain.

Seminal research on timescales has primarily focused on non-human animals, particularly macaques, using electrophysiological recordings of neural activity with high temporal resolution [25, 3, 28, 20]. Yet, because of sampling limitations of electrode arrays, only sparse sets of neurons (usual from cortical regions) can be recorded from. With sparse sampling in space it is difficult to infer the large-scale spatial organization of timescale maps. This instead requires brain-wide coverage, which is not feasible with invasive electrophysiology.

In the present paper, we focus on resting functional MRI (rfMRI), which measures spontaneous fluctuations of the blood oxygen level-dependent (BOLD) signal in the absence of external stimuli, and provides noninvasive full-brain coverage of hemodynamic processes at frequencies < 0.1 Hz [29, 11]. Compared to techniques like EEG, ECoG, and MEG, which offer high temporal resolution but relatively coarse spatial resolution, rfMRI offers dense sampling in space but sparse sampling in time. While the BOLD signal does not directly measure neural activity, it reflects hemodynamic changes associated with underlying electrophysiological signals [17], providing a means to investigate high-spatial resolution timescale maps. Several studies have found that rfMRI timescale maps consistently align spatially with those from other imaging modalities across human and animal models [29, 34, 18, 23, 15, 41, 35, 20, 14, 26].

1.2 Methodological Motivation

Neural timescales are generally estimated in the 1) time domain, 2) autocorrelation domain, or 3) frequency domain. The most common is the **autocorrelation domain**, as introduced by Murray et al. [25], where the timescale is defined by a nonlinear exponential decay fit of the sample autocorrelation function (ACF) [31, 3, 14, 32, 42, 28, 39, 26, 19, 16, 34]. Similar methods exist to characterize area under the ACF [41, 20, 40] or the time lag where the ACF crosses a predefined threshold [43, 29, 8]. Alternatively, it is possible to fit timescales directly in the **time domain** with a linear first order autoregressive model (AR1) [15, 22, 13, 18, 35, 34]; which closely reflects the exponential decay model [25] but is computationally more efficient and therefore scalable to high-dimensional applications like rfMRI. Further, time domain linear models have higher test-retest reliability than autocorrelation domain nonlinear models for rfMRI datasets [13, 18]. Lastly, the **frequency domain** approach was developed to account for neural oscillations, as timescales are properties of the aperiodic component of the signal and can be biased when the process has periodic or oscillatory components [4, 6]. These components can be more easily estimated and removed in the frequency domain, and this approach involves fitting the residual power spectral density (PSD) shape with a nonlinear Lorentzian function or measuring low frequency power to infer timescales [6, 21, 42, 5]. Given previous research showing that rfMRI is aperiodic and scale-free, characterized by 1/f-like spectral properties [11, 12], the present paper focuses only on the time and autocorrelation domain methods and the respective linear and nonlinear timescale models.

1.2.1 Problem Statement

From this overview it is clear that a primary challenge for timescales research in the lack of standardized model definitions and estimation methods across studies. Different research groups use varied approaches to define and calculate timescales, leading to inconsistent results and interpretations. Additionally, many parameterization methods rely on restrictive assumptions, potentially biasing timescale estimates and (more often) their standard errors. While some solutions exist for robust timescale estimators under general conditions [42, 4, 6], there is currently no method to robustly estimate the corresponding standard errors. Typically, existing papers report only point estimates without quantifying the uncertainty of these estimates, hindering inference, comparison across brain regions, and generalization across subjects or groups.

1.2.2 Proposed Solution

Focusing on the time domain linear model and autocorrelation domain nonlinear model we introduce robust estimators for the variance of timescale parameters under general assumptions, and establish their theoretical properties (bias, consistency, limiting variance). This enables the assignment of standard errors to traditional point estimates, allowing for scientific inference on timescale maps of the brain. To validate theoretical approaches, we use simulations and rfMRI from the Human Connectome Project (HCP) [38]. Simulations demonstrate that the proposed methods achieve nominal bias in estimating timescale and standard error maps. Further, application to the HCP dataset allow us to interpret estimated timescale maps within the context of established findings to ensure results are consistent with the extent literature on neural timescale organization.

2 Methods

This section details the two timescale models analyzed in this paper: the Time Domain Linear Model and Autocorrelation Domain Nonlinear Model. We present model assumptions, definitions, estimation, standard errors, and estimator properties. Following is a description of the Simulations used to validate the theoretical properties of the estimators, a Dataset Description used for method development and the estimation of rfMRI timescale maps, and an overview of the Group-level Analysis.

2.1 Assumptions

Let $\{X_t, t \in \mathbb{Z}\}$ be a discrete-time stochastic process that is **weakly stationary** and **ergodic**, and $x_t = \{x_1, x_2, \dots, x_T\}$ be a finite sample of X_t . For simplicity, assume X_t and x_t are mean zero. Stationarity implies a constant (independent of time index t) mean and variance, and autocovariances that only depend on time lag k :

$$\gamma_k = \text{cov}[X_t, X_{t-k}] = \mathbb{E}[X_t X_{t-k}]. \quad (1)$$

For analysis we use a normalized measure of the autocovariances, the **autocorrelation function (ACF)**:

$$\rho_k = \text{corr}(X_t, X_{t-k}) = (\gamma_0)^{-1}(\gamma_k). \quad (2)$$

where γ_k is the autocovariance at lag k and γ_0 is the variance. Thus, the autocorrelations of a stationary process are a function of the linear dependence between X_t and its lags. By the Cauchy-Schwarz

inequality, $|\rho_k| \leq \rho_0 = 1$ for all k , meaning that the dependence of a stationary process on its past values tends to weaken with increasing lag. However, stationarity does not impose further restrictions on this behavior, and in constant or periodic processes ρ_k may not decay.

Ergodicity imposes a stronger restriction on the dependence between observations than stationarity, yet still allows for a wide set of time series processes. Specifically, it requires mixing such that $\lim_{T \rightarrow \infty} \frac{1}{T} \sum_{k=1}^T |\rho_k| = 0$, and summability such that $\sum_{k=1}^{\infty} |\rho_k| < \infty$ [9, chapter 14.7]. Together, these conditions guarantee the ACF to decay to zero asymptotically at a rate that is absolutely summable. As the time separation between X_t and its lags X_{t-k} increases, the degree of dependence decreases, eventually reaching independence. These conditions allow us to characterize the **timescale** of the stochastic process by analyzing the rate of decay of its autocorrelations as a function of time lag.

As introduced by Murray et al. [25], the timescale of a neural process is typically approximated by a single parameter, τ , which defines the exponential decay rate of the ACF. Specifically, this parameter indicates the time lag where autocorrelations reach $1/e \approx 0.37$, known as e-folding time. This concept is analogous to the time constants of many physical systems. While it provides an intuitive description of the ‘memory’ or ‘persistence’ of that process, assuming that autocorrelations decay exponentially imposes a stricter requirement than ergodicity, which alone does not guarantee any specific type of decay (exponential, linear, damped periodic, etc.).

This highlights an important distinction between the data-generating process and the simplified parametric model used to describe the timescale over which such a process becomes decorrelated. In the present paper, we adopt broad assumptions, requiring only that the process is stationary and ergodic, to account for cases where the ACF decay may not be strictly exponential. Acknowledging that the data-generating process and the fitted model will likely be different in practice, the following sections describe robust standard errors that account for this mismatch, enabling valid inference despite specification error.

2.2 Timescale Definitions

The aim here is to describe exponential decay in autocorrelation of a stationary and ergodic process X_t by a single timescale parameter τ . We evaluate two working timescale models that are commonly applied across neuroimaging modalities (fMRI, EEG, ECoG, MEG) to estimate timescale maps of the brain.

2.2.1 Time Domain Linear Model

A **first order autoregressive model (AR1)** provides a convenient linear approximation of the dominant exponential decay pattern, which is implicit in the relationship between the AR1 structure and exponentially decaying autocorrelations, and it is used across a number of neural timescale papers [15, 22, 13, 18, 35, 34]. Note that this model can be applied to any stationary and ergodic process, even if the true data-generating process is not AR1, making the resulting fit an AR1 projection. The AR1 model:

$$X_t = \phi X_{t-1} + e_t \tag{3}$$

defines a parametric regression model where the relationship between X_t and X_{t-1} is linear with respect to the parameter ϕ . In the autocorrelation domain, it implies that the theoretical ACF decays exponentially at a rate determined by ϕ , such that $\rho_k = \phi^k$ [9, chapter 14.22]. Since the timescale τ is

defined as the e-folding time of the ACF, the timescale of an AR1 model is simply a change of variable:

$$\rho_\tau = \phi^\tau = \frac{1}{e} \quad (4)$$

$$\tau = g(\phi) = -\log(|\phi|)^{-1} \quad (5)$$

where the timescale τ is expressed as a nonlinear function of ϕ , denoted by $g(\phi)$. The absolute value $|\phi|$ is introduced to handle cases where ϕ might be negative as the logarithm is only defined for positive arguments. Thus, for a stationary process with $|\phi| < 1$, the exponential decay rate can be extrapolated directly from ϕ , with a timescale equal to the lag at which the AR1 projected ACF reaches $1/e \approx 0.37$.

The AR1 projection parameter ϕ^* is the value that minimizes the expected squared error function $S(\phi)$, also referred to as the loss or objective function:

$$S(\phi) = \mathbb{E}[(X_t - \phi X_{t-1})^2] \quad (6)$$

$$\phi^* = \operatorname{argmin}_\phi S(\phi). \quad (7)$$

$S(\phi)$ is minimized by taking its derivative with respect to ϕ , setting it to zero, and solving for ϕ^* :

$$\frac{d}{d\phi} S(\phi) = -2\mathbb{E}[X_{t-1}(X_t - \phi X_{t-1})] = 0 \quad (8)$$

Differentiating this quadratic function yields a linear equation in ϕ , and solving this results in a closed-form expression for the optimal ϕ^* . Therefore, ϕ^* is defined by **linear projection** and the timescale parameter τ^* by a change of variable:

$$\phi^* = (\mathbb{E}[X_{t-1}^2])^{-1}(\mathbb{E}[X_t X_{t-1}]) \quad (9)$$

$$\tau^* = g(\phi^*) = -\log(|\phi^*|)^{-1} \quad (10)$$

Importantly, we do not assume that X_t strictly follows an AR1 process with *iid* errors ($e_t \stackrel{\text{iid}}{\sim} (0, \sigma^2)$), and this flexibility allows for projection errors that may exhibit unequal variance and residual autocorrelation. Relaxing the constraints on the errors allows for approximating AR1 models where deviations from true AR1 processes are captured by the error term. And since X_t is stationary with finite variance, the parameters ϕ^* and τ^* defined by projection are unique; in fact, any approximating AR1 model is identifiable if $\mathbb{E}[X_{t-1}^2]$ is non-negative [9, theorem 14.28].

2.2.2 Autocorrelation Domain Nonlinear Model

Alternatively, the timescale model could be applied directly in the autocorrelation domain using an exponential decay fit of the ACF, as first introduced by Murray et al. [25] and cited by numerous papers [31, 3, 14, 32, 42, 28, 39, 26, 19, 16, 34]. For consistent notation with the Time Domain Linear Model above, we write the autocorrelation domain nonlinear model as:

$$\rho_k = \phi^k + e_k, \text{ for } k \in \{0, 1, \dots, K\}, \quad (11)$$

where ρ_k denotes the autocorrelation at lag k and e_k is the error term. The relationship between ρ_k and k is nonlinear in the parameter ϕ which determines the exponential decay. Note that this definition is nearly identical to the Time Domain Linear Model, in that both models describe exponential decay in autocorrelation, except that the present model defines decay across multiple (K) lags of the ACF where the AR1 model uses one lag. This subtle distinction affects the parameterization of ϕ . Thus, fitting the model in the autocorrelation domain changes its definition.

The projection parameter ϕ^* is again the value that minimizes the expected squared error function $S(\phi)$:

$$S(\phi) = \mathbb{E}[(\rho_k - \phi^k)^2] \quad (12)$$

$$\phi^* = \operatorname{argmin}_{\phi} S(\phi) \quad (13)$$

$S(\phi)$ is minimized by taking its derivative with respect to ϕ , setting it to zero, and solving for ϕ :

$$\frac{d}{d\phi} S(\phi) = -2\mathbb{E}[(k\phi^{k-1})(\rho_k - \phi^k)] = 0 \quad (14)$$

However, the derivative is nonlinear in ϕ , preventing a closed-form solution for least squares minimization. Therefore, optimization methods are needed to approximate ϕ^* by **nonlinear projection**. The corresponding timescale (e-folding time) can be expressed by a change of variable:

$$\phi^* \approx \operatorname{argmin}_{\phi} S(\phi) \quad (15)$$

$$\tau^* = g(\phi^*) = -\log(|\phi^*|)^{-1} \quad (16)$$

2.3 Timescale Estimation

2.3.1 Time Domain Linear Least Squares Estimator

The **linear least squares estimator** of the Time Domain Linear Model has the following closed-form expression:

$$\hat{\phi}_{LLS} = \left(\sum_{t=2}^T x_{t-1}^2 \right)^{-1} \left(\sum_{t=2}^T x_t x_{t-1} \right) \quad (17)$$

$$\hat{\tau}_{LLS} = g(\hat{\phi}_{LLS}) = -\log(|\hat{\phi}_{LLS}|)^{-1}, \quad (18)$$

where $\hat{\phi}_{LLS}$ is the linear least squares estimator of an AR1 model [9, chapter 14.3], and $\hat{\tau}_{LLS}$ is the timescale estimator.

2.3.2 Autocorrelation Domain Nonlinear Least Squares Estimator

Given that the Autocorrelation Domain Nonlinear Model is fit to the ACF, we first transform the time series data into the autocorrelation domain. The sample ACF for a stationary and ergodic series $x_t = \{x_1, x_2, \dots, x_T\}$, assuming it is centered, is estimated by:

$$\hat{\rho}_k = (\hat{\gamma}_0)^{-1}(\hat{\gamma}_k) = \left(\sum_{t=1}^T x_t^2 \right)^{-1} \left(\sum_{t=k+1}^T x_t x_{t-k} \right), \quad (19)$$

where $\hat{\gamma}_k$ is the sample covariance at lag k and $\hat{\gamma}_0$ is the sample variance.

The Autocorrelation Domain Nonlinear Model depends on the theoretical ACF from equation (2), which by ergodicity diminishes to zero as lag k increases. However, due to sampling variability, non-zero autocorrelations will occur when the true value is zero. To mitigate this, the ACF estimator imposes a bias towards zero by scaling the autocovariances ($\hat{\gamma}_k$, calculated using $T - k$ terms) by the total sample variance ($\hat{\gamma}_0$, calculated using all T timepoints).

The **nonlinear least squares** estimator falls in the class of optimization methods. The exponential decay parameter ϕ^* that minimizes the cost function, $S(\phi)$ in equation (15), is estimated by minimizing the sample analog $\hat{S}(\phi)$:

$$\hat{S}(\phi) = \frac{1}{K} \sum_{k=0}^K (\hat{\rho}_k - \phi^k)^2 \quad (20)$$

$$\hat{\phi}_{\text{NLS}}^* = \underset{\phi}{\operatorname{argmin}} \hat{S}(\phi) \quad (21)$$

$$\hat{\tau}_{\text{NLS}}^* = g(\hat{\phi}_{\text{NLS}}^*) = -\log(|\hat{\phi}_{\text{NLS}}^*|)^{-1}. \quad (22)$$

In this paper we use the Levenberg-Marquart algorithm to iteratively update the estimate of $\hat{\phi}_{\text{NLS}}^*$ until convergence (i.e., when the step size is below a 10^{-6} tolerance).

2.4 Standard Error Definitions

2.4.1 Time Domain Linear Model

In addition to the timescale parameter τ^* , we provide an expression for its standard error under general conditions, such as when the data-generating process is not AR1. Assuming that X_t is stationary and ergodic, so too are the model errors from equation (3) ($e_t = X_t - \phi X_{t-1}$), so we can define a standard error knowing that the autocorrelation of the errors will decay to zero asymptotically (see Assumptions). Further, since the timescale τ^* can be expressed as a nonlinear function of ϕ^* , denoted $g(\phi^*)$ in equation (16), with first partial derivative $\frac{d}{d\phi}g(\phi^*)$, the delta method can approximate its standard error:

$$\text{se}_{\text{NW}}(\phi^*) = \sqrt{q^{-1} \omega q^{-1}} \quad (23)$$

$$\text{se}_{\text{NW}}(\tau^*) \approx \text{se}_{\text{NW}}(\phi^*) \cdot \frac{d}{d\phi}g(\phi^*), \quad (24)$$

where

$$q = \mathbb{E}[X_{t-1}^2] \quad \text{and} \quad \omega = \sum_{\ell=-\infty}^{\infty} \mathbb{E}[(X_{t-1} \cdot e_t)(X_{t-1-\ell} \cdot e_{t-\ell})]. \quad (25)$$

The expression takes a sandwich form, as described by Newey and West [27], for 'heteroskedasticity and autocorrelation consistent (HAC)' standard errors [9, theorem 14.32]. This formula explicitly adjusts for misspecification by accounting for the covariance structure of the errors, which ensures that the standard errors are asymptotically correct (see (46)). The covariance terms in ω capture deviations in the error structure from the standard *iid* case. For the special case of correct specification, when X_t is a true AR1 process, the standard error of the AR1 coefficient ϕ^* reduces to:

$$\text{se}_{\text{Naive}}(\phi^*) = \sqrt{\sigma^2 q^{-1}} \quad (26)$$

where σ^2 is the error variance.

This framework can approximate a general class of decay processes as exponential with standard errors that are robust to model misspecification. Importantly, it allows for the construction of asymptotic approximations, confidence intervals, and null hypothesis tests. Therefore, inferences can be made even when the AR1 model is incorrect.

2.4.2 Autocorrelation Domain Nonlinear Model

Although the model defines a parametric regression function with an exponential decay form, it can accommodate deviations from this decay pattern by incorporating the error term from equation (11) ($e_k = \rho_k - \phi^k$), allowing for more general stationary and ergodic processes. Following the description in Hansen [9, chapter 22.8, chapter 23.5], if ϕ^* uniquely minimizes $S(\phi)$, such that $S(\phi) > S(\phi^*)$ for all $\phi \neq \phi^*$, the standard error of ϕ^* can be computed using a sandwich form that reflects both the curvature of the squared loss function at its minimum and the covariance of the errors. Furthermore, since the timescale τ is a nonlinear function of ϕ^* , represented by $g(\phi^*)$, the delta method can provide an approximation of its standard error:

$$\text{se}_{\text{NW}}(\phi^*) = \sqrt{q^{-1} \omega q^{-1}} \quad (27)$$

$$\text{se}_{\text{NW}}(\tau^*) \approx \text{se}_{\text{NW}}(\phi^*) \cdot \frac{d}{d\phi} g(\phi^*). \quad (28)$$

The components q and ω are derived from the regression function $m(k, \phi) = \phi^k$ and its derivative $m_{\phi,k} = \frac{d}{d\phi} m(k, \phi) = k\phi^{k-1}$, defined as:

$$q = \mathbb{E}[m_{\phi^*,k}^2] = \mathbb{E}[(k\phi^{*k-1})^2] \quad \text{and} \quad \omega = \sum_{\ell=-\infty}^{\infty} \mathbb{E}[(m_{\phi^*,k} \cdot e_k)(m_{\phi^*,k-\ell} \cdot e_{k-\ell})]. \quad (29)$$

The derivative of the regression function evaluated at ϕ^* ($m_{\phi^*,k}$) is a linearized regressor, and used to locally approximate the nonlinear model by a linear one. As with the time domain linear model (equation (23)), this form ensures that the standard errors are asymptotically valid even with model deviations (see (51)). This is a realistic scenario under the mild conditions of stationarity and ergodicity. In the special case where the errors are *iid*, $e_k \stackrel{\text{iid}}{\sim} (0, \sigma^2)$, the standard error of ϕ^* simplifies to:

$$\text{se}_{\text{Naive}}(\phi^*) = \sqrt{\sigma^2 q^{-1}} \quad (30)$$

2.5 Standard Error Estimation

2.5.1 Time Domain Newey-West Estimator

If the data-generating process is not AR1 and the errors have positive autocorrelation, while it does not bias the estimates of $\hat{\phi}_{\text{LLS}}$ or $\hat{\tau}_{\text{LLS}}$, the standard errors will be underestimated (and the t-scores overestimated). To consistently estimate the standard errors for more general processes we apply the Newey-West sandwich formula, and the delta method [27]:

$$\widehat{\text{se}}_{\text{NW}}(\hat{\phi}_{\text{LLS}}^*) = \sqrt{\hat{q}^{-1} \hat{\omega} \hat{q}^{-1}} \quad (31)$$

$$\widehat{\text{se}}_{\text{NW}}(\hat{\tau}_{\text{LLS}}^*) \approx \widehat{\text{se}}_{\text{NW}}(\hat{\phi}_{\text{LLS}}^*) \cdot \frac{d}{d\phi} g(\hat{\phi}_{\text{LLS}}^*) \quad (32)$$

where

$$\hat{q} = \frac{1}{T} \sum_{t=2}^T x_{t-1}^2 \quad \text{and} \quad \hat{\omega} = \sum_{\ell=-M}^M \left(1 - \frac{|\ell|}{M+1}\right) \frac{1}{T} \sum_{1 \leq t-\ell \leq T} (x_{t-1} \cdot \hat{e}_t)(x_{t-1-\ell} \cdot \hat{e}_{t-\ell}). \quad (33)$$

This estimator calculates a weighted sum of the regression scores $x_{t-1} \cdot \hat{e}_t$, where $\hat{e}_t = x_t - \hat{\phi}_{\text{LLS}}^* \cdot x_{t-1}$. The true ω is approximated by $\hat{\omega}$ by taking a finite sum of the regression score autocovariances up to lag M , where M is the lag-truncation (or bandwidth). The weights used in the sum decrease linearly with lag ℓ , following a Bartlett kernel. This kernel not only ensures the standard errors remain non-negative but also regularizes $\hat{\omega}$ to change smoothly with M [9, chapter 14.35].

Although an unlikely scenario when working with real data, for completeness we also include the naive estimator which simplifies under the assumption that x_t is an AR1 process. The simplified form is:

$$\widehat{\text{se}}_{\text{Naive}}(\hat{\phi}_{\text{LLS}}) = \sqrt{\hat{\sigma}^2 \hat{q}^{-1}} \quad (34)$$

$$\widehat{\text{se}}_{\text{Naive}}(\hat{\tau}_{\text{LLS}}) = \widehat{\text{se}}_{\text{Naive}}(\hat{\phi}_{\text{LLS}}) \frac{d}{d\phi} g(\hat{\phi}_{\text{LLS}}) \quad (35)$$

where $\hat{\sigma}^2 = \frac{1}{T} \sum_{t=2}^T \hat{e}_t^2$ is an estimate of the error variance.

2.5.2 Autocorrelation Domain Newey-West Estimator

The variability of $\hat{\phi}_{\text{NLS}}^*$ at the point of convergence is assessed using a sandwich estimator of the standard error. This approach involves the linearized regressor — defined as the derivative of the regression function with respect to ϕ , evaluated at the estimated parameter $\hat{\phi}_{\text{NLS}}^*$ — used as a local linear approximation of the nonlinear model. This approximation facilitates the calculation of standard errors, quantifying the uncertainty in both the location of the regression function and the precision of the parameter estimate. The standard error of the timescale is again approximated by the delta method:

$$\widehat{\text{se}}_{\text{NW}}(\hat{\phi}_{\text{NLS}}^*) = \sqrt{\hat{q}^{-1} \hat{\omega} \hat{q}^{-1}} \quad (36)$$

$$\widehat{\text{se}}_{\text{NW}}(\hat{\tau}_{\text{NLS}}^*) \approx \widehat{\text{se}}_{\text{NW}}(\hat{\phi}_{\text{NLS}}^*) \cdot \frac{d}{d\phi} g(\hat{\phi}_{\text{NLS}}^*) \quad (37)$$

where

$$\hat{q} = \frac{1}{K} \sum_{k=0}^K (\hat{m}_{\phi,k})^2 = \frac{1}{K} \sum_{k=0}^K (k \hat{\phi}_{\text{NLS}}^{*k-1})^2, \quad (38)$$

$$\hat{\omega} = \sum_{\ell=-M}^M \left(1 - \frac{|\ell|}{M+1}\right) \frac{1}{K} \sum_{1 \leq k-\ell \leq K} (\hat{m}_{\phi,k} \cdot \hat{e}_k) (\hat{m}_{\phi,k-\ell} \cdot \hat{e}_{k-\ell}). \quad (39)$$

This estimator calculates a weighted sum of the linearized regression scores $\hat{m}_{\phi,k} \cdot \hat{e}_k$ where $\hat{e}_k = \hat{\rho}_k - (\hat{\phi}_{\text{NLS}}^*)^k$. The estimate of $\hat{\omega}$ takes a finite sum of these scores up to lag M , weighted by a Bartlett kernel, so that $\hat{\omega}$ changes smoothly with M .

As discussed previously, naive standard errors will likely be biased downward in practical applications, rendering invalid confidence intervals or hypothesis tests that rely on them. However, in the case of correct specification, the equation simplifies to:

$$\widehat{\text{se}}_{\text{Naive}}(\hat{\phi}_{\text{NLS}}^*) = \sqrt{\hat{\sigma}^2 \hat{q}^{-1}} \quad (40)$$

$$\widehat{\text{se}}_{\text{Naive}}(\hat{\tau}_{\text{NLS}}^*) \approx \widehat{\text{se}}_{\text{Naive}}(\hat{\phi}_{\text{NLS}}^*) \frac{d}{d\phi} g(\hat{\phi}_{\text{NLS}}^*) \quad (41)$$

where $\hat{\sigma}^2 = \frac{1}{K} \sum_{k=0}^K \hat{e}_k^2$ is an estimate of the error variance.

2.6 Estimator Properties

In this section, we describe the large-sample properties of both the Time Domain Linear Model and Autocorrelation Domain Nonlinear Model, focusing on the consistency and limiting variance of their respective estimators. Under general conditions — such as when the linear model is applied to a process that is not AR(1), or the nonlinear model is applied to a decay process that is not strictly exponential — we demonstrate that the asymptotic distribution remains Gaussian, with a limiting variance that can be consistently estimated. Consequently, the resulting t-ratios (see equation (66)) are also asymptotically Gaussian. This allows for the construction of hypothesis tests and confidence intervals across timescale maps of the brain.

2.6.1 Time Domain Linear Least Squares Estimator

Following the description in Hansen [9, theorem 14.29], the ergodic theorem shows that ergodicity is a sufficient condition for **consistent estimation**. Since X_t is stationary and ergodic, so too are $X_t X_{t-1}$ and X_{t-1}^2 , and as $T \rightarrow \infty$:

$$\frac{1}{T} \sum_{t=2}^T x_t x_{t-1} \xrightarrow{p} \mathbb{E}[X_t X_{t-1}] \quad (42)$$

$$\frac{1}{T} \sum_{t=2}^T x_{t-1}^2 \xrightarrow{p} \mathbb{E}[X_{t-1}^2]. \quad (43)$$

Applying the continuous mapping theorem yields:

$$\hat{\phi}_{\text{LLS}}^* = \left(\frac{1}{T} \sum_{t=2}^T x_{t-1}^2 \right)^{-1} \left(\frac{1}{T} \sum_{t=2}^T x_t x_{t-1} \right) \xrightarrow{p} (\mathbb{E}[X_{t-1}^2])^{-1} (\mathbb{E}[X_t X_{t-1}]) = \phi^*. \quad (44)$$

This shows that the coefficients of the Time Domain Linear Model can be consistently estimated by least squares, for any stationary and ergodic process with parameters defined by projection (equation (9)). Similarly:

$$\hat{\omega} \xrightarrow{p} \omega \quad (45)$$

Further, the asymptotic distribution under general dependence states that the **limiting variance** of ϕ can be approximated using a central limit theorem for correlated observations as $T \rightarrow \infty$ Hansen [9, theorem 14.33]:

$$\frac{\hat{\phi}_{\text{LLS}}^* - \phi^*}{\widehat{\text{se}}_{NW}(\hat{\phi}_{\text{LLS}}^*)} \xrightarrow{d} \mathcal{N}(0, 1). \quad (46)$$

And by the delta method we obtain the limiting variance for the timescale τ :

$$\frac{\hat{\tau}_{\text{LLS}}^* - \tau^*}{\widehat{\text{se}}_{NW}(\hat{\phi}_{\text{LLS}}^*) \cdot \frac{d}{d\phi} g(\hat{\phi}_{\text{LLS}}^*)} \xrightarrow{d} \mathcal{N}(0, 1). \quad (47)$$

2.6.2 Autocorrelation Domain Nonlinear Least Squares Estimator

To show **consistent estimation**, unlike the time domain linear model above where we apply the ergodic theorem to the explicit closed-form expression of the estimator, this is not possible for nonlinear estimators because there is no algebraic expression. Instead, nonlinear least squares minimizes the sample objective function $\widehat{S}(\phi)$, which is itself a sample average. By Hansen [9, theorem 22.1], for any ϕ , the weak law of large numbers shows that:

$$\widehat{S}(\phi) \xrightarrow{p} S(\phi). \quad (48)$$

Further, if the minimizer ϕ^* is unique, $S(\phi) > S(\phi^*)$ for all $\phi \neq \phi^*$, then the sample minimizer converges in probability to the true minimum as $K \rightarrow \infty$:

$$\hat{\phi}_{\text{NLS}}^* \xrightarrow{p} \phi^* \quad (49)$$

This shows that the parameters of the Autocorrelation Domain Nonlinear Model can be consistently estimated by least squares. Similarly:

$$\hat{\omega} \xrightarrow{p} \omega \quad (50)$$

With the additional assumption that the objective function is Lipschitz-continuous for ϕ near ϕ^* , following Hansen [9, theorem 23.2], we can approximate the **limiting variance** of ϕ and τ using a central limit theorem for correlated observations. Under general conditions, the nonlinear least squares estimator has an asymptotic distribution with a similar structure to that of the linear least squares estimator above; it converges to a Gaussian distribution with a sandwich-form variance:

$$\frac{\hat{\phi}_{\text{NLS}}^* - \phi^*}{\widehat{\text{se}}_{NW}(\hat{\phi}_{\text{NLS}}^*)} \xrightarrow{d} \mathcal{N}(0, 1). \quad (51)$$

And by the delta method we obtain the limiting variance for the timescale τ :

$$\frac{\hat{\tau}^* - \tau^*}{\widehat{\text{se}}_{NW}(\hat{\phi}_{\text{NLS}}^*) \cdot \frac{d}{d\phi} g(\hat{\phi}_{\text{NLS}}^*)} \xrightarrow{d} \mathcal{N}(0, 1) \quad (52)$$

2.7 Simulations

The performances of the Time Domain Linear Model and Autocorrelation Domain Nonlinear Model were evaluated using Monte Carlo simulations, with $N = 10,000$ independent replications tested in each setting. For the time domain model, we simulated time series realizations $x_t = \{x_1, x_2, \dots, x_T\}$ with $T = 4800$, and Gaussian white noise errors, $e_t \stackrel{\text{iid}}{\sim} \mathcal{N}(0, 1)$. To test the autocorrelation domain model, we simulated autocorrelation functions (ACFs) $\rho_k = \{\rho_0, \rho_1, \dots, \rho_K\}$ with $K = 300$, also with Gaussian white noise errors, $e_k \stackrel{\text{iid}}{\sim} \mathcal{N}(0, 1)$. The empirical bias and standard error of parameter estimates were compared to true values to evaluate estimator performance in terms of sampling bias and variance.

We simulated x_t and ρ_k based on three distinct data-generating models, each characterized by a different autocorrelation structure: AR1, AR2, and autocorrelations derived from rfMRI data (see Dataset Description). In all cases, the autocorrelation structures were constrained to have the same AR1 projection parameters (ϕ_{AR1}), ensuring comparable timescales across settings. That is, there is always a ϕ_{AR1} value that represents the AR1 projection, even if the time series was generated by a more complex process. To define a feasible parameter range for simulation, we referred to the Human Connectome Project dataset, where empirical results produced only positive parameter estimates; accordingly, the range of simulated parameters was restricted to positive values. The strength of the autocorrelations was varied by selecting five fixed ϕ_{AR1} values, evenly spaced between 0.1 – 0.8. This design resulted in a total of 15 simulation settings (3 data-generating models \times 5 autocorrelation strengths). The corresponding timescales follow the nonlinear transformation in equation (5):

$$\phi_{\text{AR1}} \in \{0.1, 0.275, 0.45, 0.625, 0.8\} \quad (53)$$

$$\tau_{\text{AR1}} \in \{0.43, 0.78, 1.25, 2.13, 4.48\}. \quad (54)$$

The **AR1 setting** is the only case where the data-generating process aligns with the fitted model in both the time and autocorrelation domains. To simulate data, the time series were generated from a first-order autoregressive process and the ACFs by an exponential decay process:

$$x_t = \phi x_{t-1} + e_t \quad (55)$$

$$\rho_k = \phi^k + e_k. \quad (56)$$

The **AR2 setting** introduces a discrepancy between the data-generating process (AR2) and the fitted model (AR1). While still a linear process, AR2 allows for more complex stochastic dynamics. Depending on the parameter values, AR2 processes can produce a variety of behaviors, including periodic signals with ACFs that decay as damped cosines or mixtures of decaying exponentials. However, in this study, the dataset lacked oscillatory characteristics — a feature typically absent in rfMRI signals, as shown in previous work [11]. As a result, the simulations were limited to stationary and aperiodic AR2 processes, with five pairs of AR2 coefficients selected so that the AR1 projections matched the timescales defined earlier (equation (53)):

$$(\phi_1, \phi_2) \in \{(0.09, 0.09), (0.23, 0.18), (0.35, 0.23), (0.47, 0.24), (0.65, 0.19)\} \quad (57)$$

$$\tau_{\text{AR1}} \in \{0.43, 0.78, 1.25, 2.13, 4.48\}. \quad (58)$$

The following models were used to simulate AR2 time and autocorrelation processes:

$$x_t = \phi_1 x_{t-1} + \phi_2 x_{t-2} + e_t \quad (59)$$

$$\rho_k = \phi_1 \rho_{k-1} + \phi_2 \rho_{k-2} + e_k. \quad (60)$$

The **HCP setting** did not follow an autoregressive process, using instead empirical autocorrelation structures from five brain regions # $\{7, 12, 126, 137, 143\}$ of subject #100610 from the HCP dataset. These regions were selected to match the AR1 projections of the predefined timescale values (equation (53)). To simulate time series with the same autocorrelation structure as the empirical data, we sampled from a multivariate normal distribution $\mathcal{N}(0, \hat{\Sigma})$, where $\hat{\Sigma} \in \mathbb{R}^{K \times K}$ is the covariance matrix constructed from the sample ACF of each region. Under stationarity, the covariance matrix $\hat{\Sigma}$ has a Toeplitz structure, meaning its k^{th} off-diagonal elements represent the sample ACF at lag k : $\hat{\Sigma}_{i-k,j-k} = \hat{\Sigma}_{i+k,j+k} = \hat{\rho}_k$. To generate the time series, we applied the Cholesky decomposition $\hat{\Sigma} = LL^\top$, where L is a lower triangular matrix, and multiplied it by Gaussian white noise to produce a time series with the desired autocorrelation:

$$x_t = Le_t. \quad (61)$$

Lastly, for testing the autocorrelation domain model, the true ACF was treated as the estimated ACF with an added noise term:

$$\rho_k = \hat{\rho}_k + e_k \quad (62)$$

2.8 Dataset Description

Resting fMRI (rfMRI) scans were provided by the Human Connectome Project (HCP), WU-Minn Consortium (led by principal investigators David Van Essen and Kamil Ugurbil; 1U54MH091657) funded by the 16 NIH Institutes and Centers supporting the NIH Blueprint for Neuroscience Research, and by the McDonnell Center for Systems Neuroscience at Washington University [38]. The present paper used two subsets of the larger dataset: one for method development and defining realistic simulation parameters (see Simulations), and the other for estimating high-resolution timescale maps of the cortex.

For development, we used the first ten subjects (#100004 - #101410) with rfMRI scans acquired using a 3-tesla gradient-echo EPI sequence (TR=720ms, TE=33.1ms, flip angle=52°, FOV=208x180mm, slice thickness=2.0mm) [38]. Subjects were awake with their eyes open focused on a fixation cross projected on a dark background for four runs (15 minutes each, T=4800 total timepoints). Minimal preprocessing was applied to each run, detailed in [7]. This included anatomical surface reconstruction [30] and functional data registered to grayordinates (a spatial map including surface vertices and subcortical gray matter voxels). Additionally, functional time series were preprocessed by applying high-pass filtering, regression of head motion parameters, and removal of temporal artifacts detected by the FIX algorithm [33]. This ensured the removal of nonstationary signal drift and noise (e.g., movement, physiological confounds). To reduce dimensionality, we took weighted spatial averages within 300 brain regions defined by a group-level independent component analysis (ICA) atlas [36]. This yielded a dataset with the dimensions {10 subjects, 4800 timepoints, 300 regions}.

For estimating timescale maps, we used the subset of 180 HCP subjects with rfMRI scans acquired with a 7-tesla gradient-echo EPI sequence (TR=1000ms, TE=22.2ms, flip angle=45°, FOV=208 x 208mm, slice thickness=1.6 mm) [38, 24]. This sequence offers the highest available spatial resolution for human rfMRI, and allows for mapping at the order of 1.6mm². Four runs of 16 minutes (3600 total timepoints) were collected using the same eyes-open fixation protocol. Preprocessing mirrored that which is described above. However, functional data were analysed on the grayordinate map downsampled to 2mm, yielding a dataset with the dimensions {180 subjects, 3600 timepoints, 91282 grayordinates}. We independently fit the Time Domain Linear Model and Autocorrelation Domain Nonlinear Model to each grayordinate, a mass-univariate analysis approach that resulted in subject-level maps of timescale estimates and their standard errors.

2.9 Group-level Analysis

For group-level maps, the timescale estimates and standard errors were combined to account for both within-individual variability and between-individual variability. While remaining within the mass-univariate framework, for simplicity, we express the group timescale for the $N = 180$ individual subjects at a single grayordinate:

$$\hat{\tau}_n \text{ for } n \in \{1, 2, \dots, N\} \quad (63)$$

$$\hat{\tau}_N = \frac{1}{N} \sum_{n=1}^N \hat{\tau}_n. \quad (64)$$

By the law of total variance, the group-level standard error for the timescale is estimated by:

$$\widehat{\text{se}}(\hat{\tau}_N) = \sqrt{\frac{1}{N} \sum_{n=1}^N \widehat{\text{se}}(\hat{\tau}_n)^2 + \frac{1}{N} \sum_{n=1}^N (\hat{\tau}_n - \hat{\tau}_N)^2}. \quad (65)$$

Here, the first term under the square root is the within-individual variance and the second term is the between-individual variance.

To visualize timescales on the brain, statistical parametric maps were constructed using **t-statistics** at each grayordinate. These t-statistics specifically tested whether timescales exceeded a half second ($H_0 : \tau \leq 0.5$ sec.), computed as the ratio:

$$t_N = \frac{\hat{\tau}_N - 0.5}{\widehat{\text{se}}(\hat{\tau}_N)}. \quad (66)$$

Additionally, maps of **relative standard errors** were used to visualize the spatial distribution in the precision and reliability of timescale estimates across the brain, using the ratio:

$$\text{rse}(\hat{\tau}_N) = \frac{\widehat{\text{se}}(\hat{\tau}_N)}{\hat{\tau}_N} \quad (67)$$

3 Results

This section presents simulation results and timescale maps from resting fMRI (rfMRI). It compares the Time Domain Linear Model and Autocorrelation Domain Nonlinear Model methods in terms of timescale estimates, standard errors, t-statistics, and relative standard errors, highlighting differences in finite sample bias and variance. Three simulation settings are shown (see Simulations): AR1 1, AR2 2, and empirical 3. Additionally, brain timescale maps from the Human Connectome Project are included for an individual 4 and group 5, showing spatial patterns and reliability metrics across brain regions.

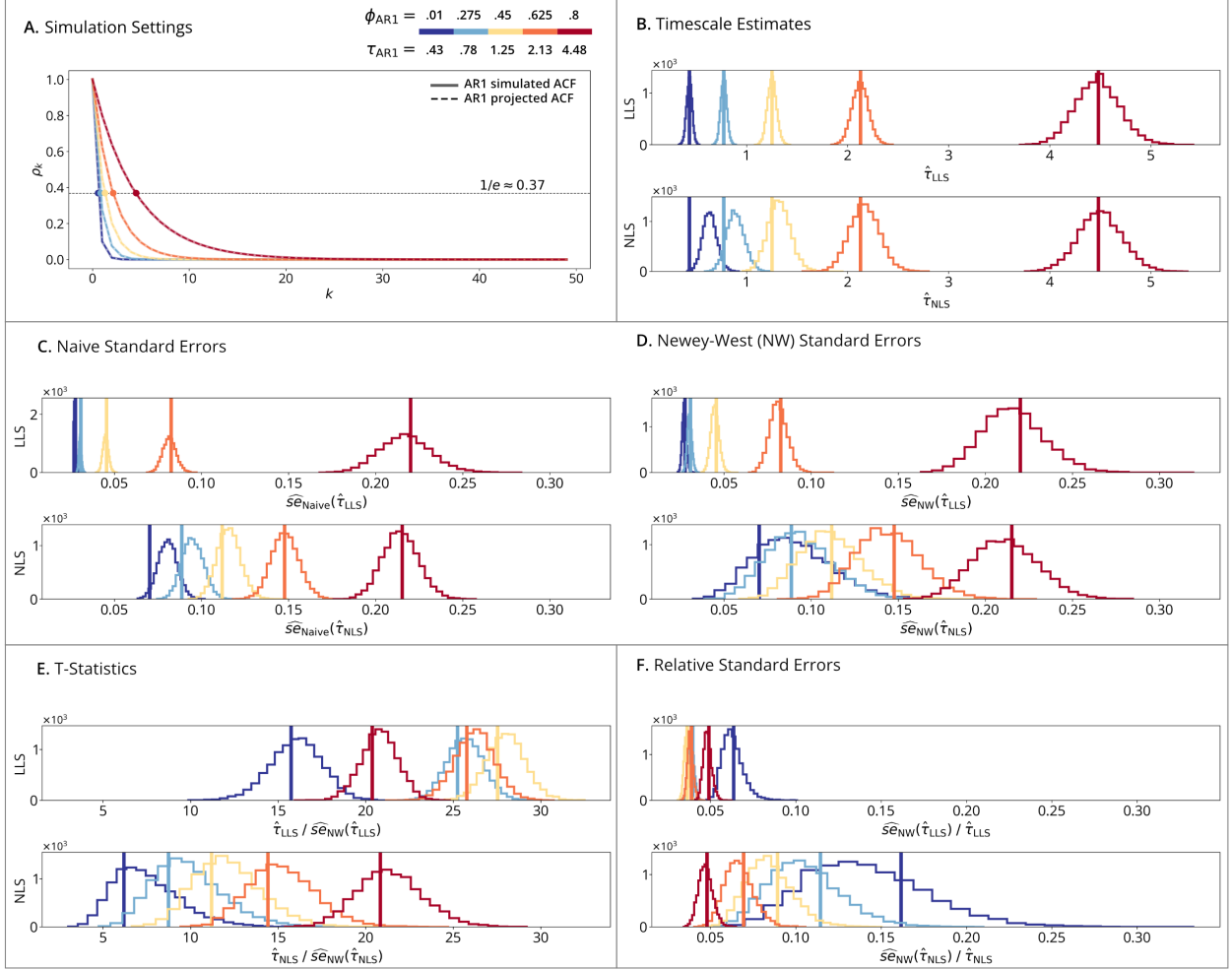


Figure 1: **AR1 simulations.** (A) Simulation Settings. Five fixed settings are illustrated, where the solid line represents the simulated autocorrelation function (ACF), and the dashed line represents the AR1-projected ACF. Since both ACFs follow AR1, they overlap. Solid dots mark the timescale at which the AR1-projected ACF reaches $1/e \approx 0.37$. (B) Timescale Estimates. Vertical lines show the true timescale parameters, and histograms show the distribution of timescale estimates across $N = 10,000$ independent replications. The top plot shows the results for the linear least squares estimator (see Time Domain Linear Model), and the bottom plot for the nonlinear least squares estimator (see Autocorrelation Domain Nonlinear Model). (C) Naive Standard Errors and (D) Newey-West Standard Errors. Vertical lines show the standard deviations of the sampling distributions from panel B, while histograms show the distribution of standard error estimates using the naive and Newey-West estimators, respectively. (E) T-Statistics and (F) Relative Standard Errors (RSEs). Vertical lines show true values and histograms show the distributions of the estimates.

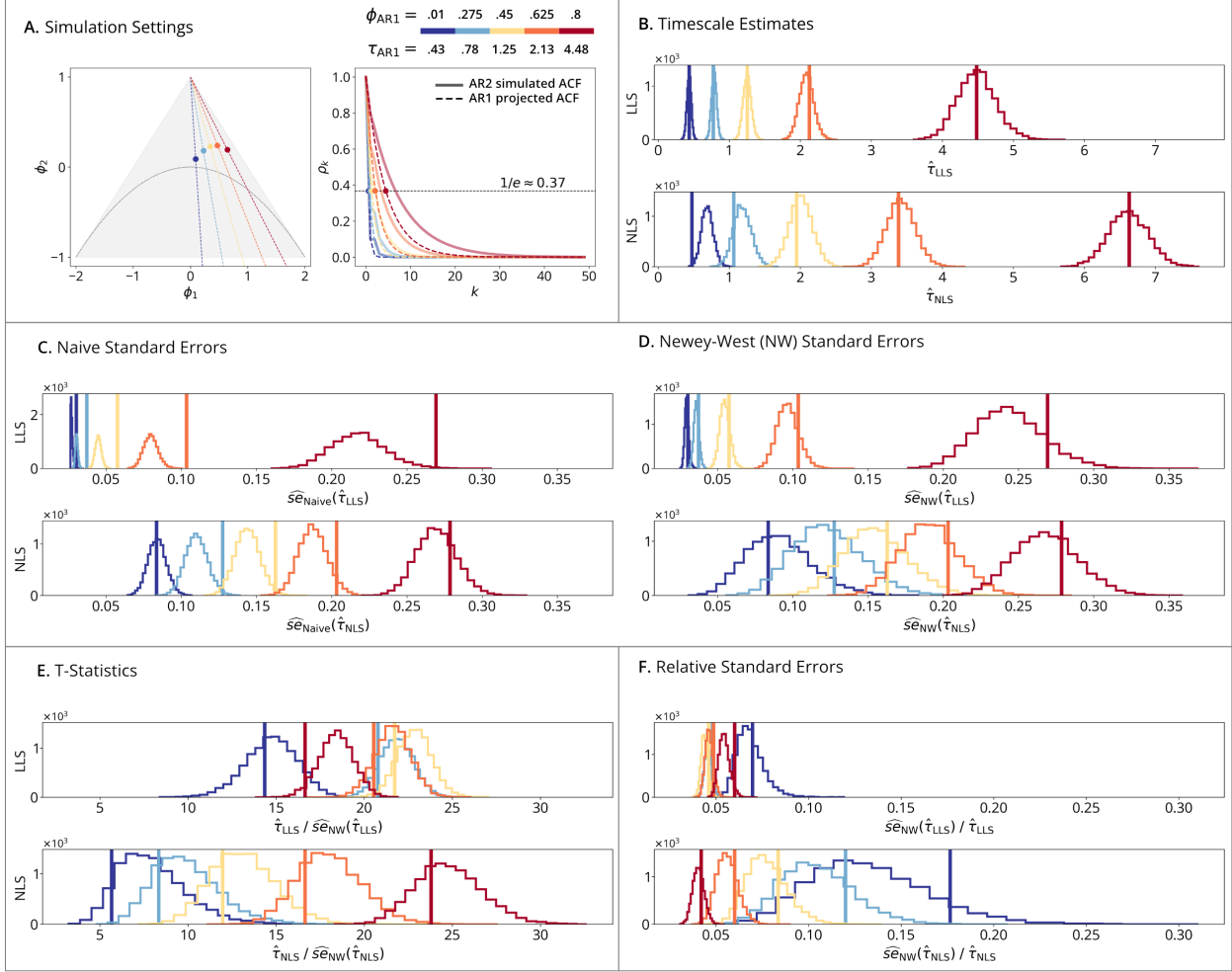


Figure 2: AR2 simulations. (A) Simulation Settings. The AR2 stationary region (gray triangle) in the (ϕ_1, ϕ_2) plane is defined by the conditions $\phi_2 < 1 + \phi_1, \phi_2 < 1 - \phi_1, \phi_2 > -1$. Within this region, the theoretical boundary between periodic and aperiodic behavior is given by $\phi_2 = -\phi_1^2/4$. Five fixed (ϕ_1, ϕ_2) pairs within the stationary and aperiodic region were used to simulate AR2 processes with AR1 projections (dashed lines) equivalent to Figure 1. In the autocorrelation domain, the solid lines represent the simulated autocorrelation function (ACF), and the dashed line represents the AR1-projected ACF. Since the simulated ACF is AR2 and the projected is AR1, the lines do not overlap. Solid dots mark the timescale at which the AR1-projected ACF reaches $1/e \approx 0.37$. (B) Timescale Estimates. Vertical lines show the true timescale parameters, and histograms show the distribution of timescale estimates across $N = 10000$ independent replications. The top plot shows the results for the linear least squares estimator (see Time Domain Linear Model), and the bottom plot for the nonlinear least squares estimator (see Autocorrelation Domain Nonlinear Model). The true values of the two estimators differ because of their respective definitions. (C) Naive Standard Errors and (D) Newey-West Standard Errors. Vertical lines show the standard deviations of the sampling distributions from panel B, while histograms show the distribution of standard error estimates using the naive and Newey-West estimators, respectively. (E) T-Statistics and (F) Relative Standard Errors (RSEs). Vertical lines show true values and histograms show the distributions of the estimates.

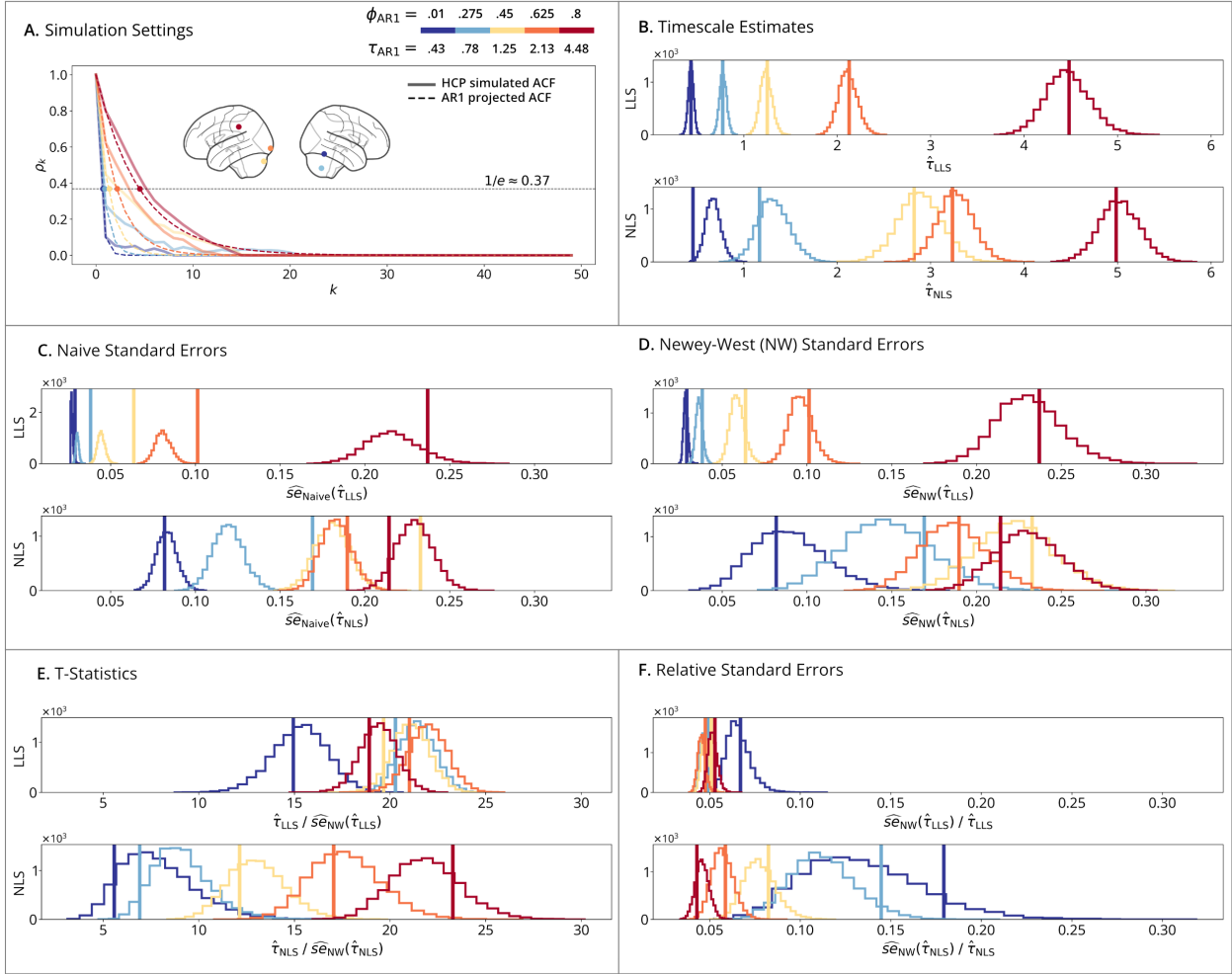


Figure 3: Realistic rfMRI simulations. (A) Simulation Settings. Five fixed settings are illustrated, where the solid line represents the simulated autocorrelation function (ACF) of the specified brain region from subject #100610 of the Human Connectome Project, and the dashed line represents the AR1-projected ACF. Since the simulated ACF depends on rfMRI data and the projected is AR1, the lines do not overlap. Solid dots mark the timescale at which the AR1-projected ACF reaches $1/e \approx 0.37$. (B) Timescale Estimates. Vertical lines show the true timescale parameters, and histograms show the distribution of timescale estimates across $N = 10000$ independent replications. The top plot shows the results for the linear least squares estimator (see Time Domain Linear Model), and the bottom plot for the nonlinear least squares estimator (see Autocorrelation Domain Nonlinear Model). The true values of the two estimators differ because of their respective definitions. (C) Naive Standard Errors and (D) Newey-West Standard Errors. Vertical lines show the standard deviations of the sampling distributions from panel B, while histograms show the distribution of standard error estimates, using the naive and Newey-West estimators, respectively. (E) T-Statistics and (F) Relative Standard Errors (RSEs). Vertical lines show true values and histograms show the distributions of the estimates.

3.1 Timescale Estimators in Autoregressive Simulations

AR1 simulation results (Figure 1) follow the setting where the data-generating process aligns with the fitted models, where each time series is generated from a first-order autoregressive process (fit by LLS) and each ACF by an exponential decay process (fit by NLS). The figure panels show how accurately the timescale estimators recover the true parameters and their standard errors as the timescale increases. **Panel B** shows that larger timescales lead to greater variability in the estimates, indicated by wider sampling distributions. Comparing the estimators, LLS remains unbiased across all timescales, while NLS exhibits upward bias at smaller timescales. **Panels C and D** compare the naive and Newey-West standard errors. Both estimators are unbiased, but standard errors increase as the timescales grow. The Newey-West estimator displays greater variability in standard error estimates compared to the naive estimator. This pattern holds for NLS as well, though the increase in variability is less pronounced, and the naive standard errors are overestimated for smaller timescales. **Panel E** examines t-statistics (signal-to-noise ratios). For LLS, the t-ratios fluctuate as timescales increase, while NLS shows a steady rise, indicating that larger timescales are easier to estimate. Across all timescales (except for the largest, $\tau_{\text{AR1}} = 4.48$), LLS outperforms NLS in terms of signal-to-noise ratios, and **Panel F** confirms that LLS also has lower RSEs. Overall, when both LLS and NLS are correctly specified they achieve nominal bias (i.e., they recover the true timescales and standard errors), though LLS is more reliable for small timescales.

AR2 simulation results (Figure 2) explore how timescale estimators perform when the data-generating model is AR2, introducing misspecification since the estimators fit AR1 projections. In this setting, the goal is to assess the impact of specification error on timescale estimation. **Panel A** illustrates the AR2 autocorrelation function (ACF) and its AR1 projection, emphasizing the mismatch between the true and fitted models. **Panel B** shows that the true timescale differs between the two estimators due to their respective definitions. Despite the misspecification, both timescale estimators remain (mostly) unbiased. However, the standard error estimates for both LLS and NLS are biased downward, particularly at larger timescales. The Newey-West estimator reduces this bias, improving the accuracy of standard error estimates for both models. **Panels E-F** show that, similar to the AR1 case, the LLS compared to the NLS estimator generally achieves larger t-statistics (indicating a higher signal-to-noise ratio) and lower RSEs. Additionally, larger timescales are easier to estimate, particularly for the LLS estimator. In summary, the Newey-West estimators can recover the true standard errors under model misspecification, larger timescales are generally easier to estimate, and the LLS estimator is more reliable for small timescales.

3.2 Timescale Estimators in Realistic rfMRI Simulations

Realistic rfMRI simulation results (Figure 3) explore the performance of timescale estimators when simulating empirical processes derived from five distinct brain regions from a single subject. Like the AR2 results described above, this simulation method is designed to test estimator performance under model misspecification, as the data-generating process reflects realistic brain dynamics, while the fitted models project a simpler AR1 process. **Panel A** shows the empirical ACFs from these brain regions alongside their AR1 projections, highlighting the mismatch between the true underlying processes and the fitted models. **Panel B** presents the timescale estimates, where the LLS and NLS estimators yield different timescales due to their respective definitions. The naive standard error estimator for LLS consistently exhibits downward bias, while the NLS naive estimator shows bias that varies in direction depending on the timescale. For both methods, the Newey-West standard error estimates mitigate these biases, though they increase the variability of the estimates, particularly for NLS. **Panels E-F** display the t-statistics and RSEs, respectively, with LLS again demonstrating more stable and lower RSEs compared to NLS across most timescales. Larger timescales are consistently easier to estimate, and the Newey-West corrections effectively reduce bias, albeit at the cost of greater variability. These re-

sults are consistent with the AR2 simulations using a setting that is more realistic for estimating rfMRI timescale maps.

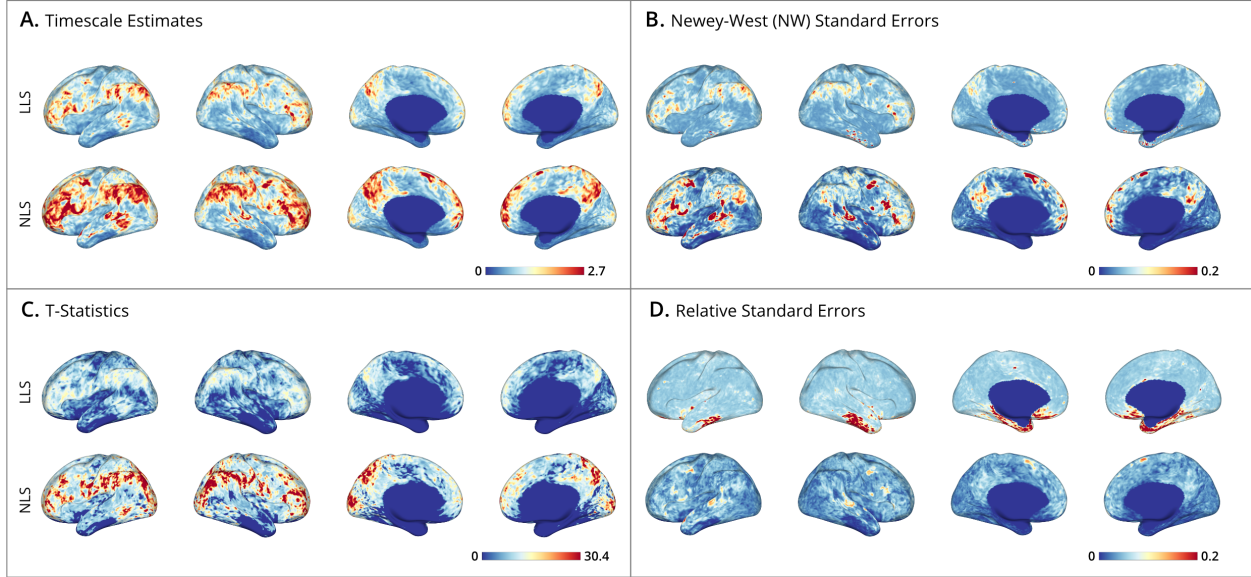


Figure 4: Human Connectome Project subject-level timescale maps. (A-D) panels display cortical gray-matter maps from subject #100610 of the Human Connectome Project (see Dataset Description). Displays include lateral-left, lateral-right, medial-left, and medial-right views (excluding the medial wall). The upper bounds on the colorbars are set for each panel at the 99th percentile of the cortical map values. For each panel, the top row shows the results of linear least squares estimator (LLS; see Time Domain Linear Model), and the bottom row shows the results of the nonlinear least squares estimator (NLS; see Autocorrelation Domain Nonlinear Model). **A** Timescale Estimates. Maps display the timescales (e-folding time in seconds) across brain regions. **B** Newey-West Standard Errors. Maps display the spatial distribution of robust standard error estimates, with smaller values indicating greater precision in the timescale estimates. **C** T-Statistics. Maps display unthresholded and uncorrected t-ratios (see (66)), testing whether timescales at each grayordinate exceed a half second. **D** Relative Standard Errors (RSEs). Values show the relative reliability of timescale estimates across brain regions. Low RSE (near zero) indicates high precision with small uncertainty, while higher RSE reflects lower reliability of the estimates.

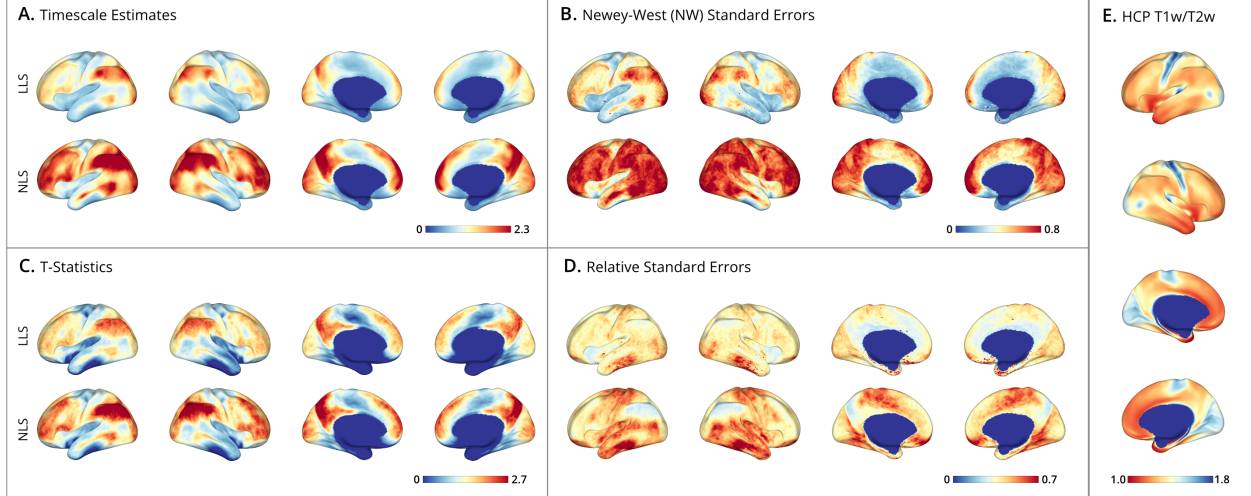


Figure 5: Human Connectome Project group-level timescale maps. (A-D) panels display cortical gray-matter maps from the group of $N = 180$ subjects in the Human Connectome Project dataset (see Dataset Description). Displays include lateral-left, lateral-right, medial-left, and medial-right views (excluding the medial wall). The upper bounds on the colorbars are set for each panel at the 99th percentile of the cortical map values. The top row in each panel shows results from the linear least squares estimator (LLS; see Time Domain Linear Model), and the bottom row shows results from the nonlinear least squares estimator (NLS; see Autocorrelation Domain Nonlinear Model). **A** Timescale Estimates. Maps display the group-level timescales (e-folding time in seconds) across brain regions, averaged over subjects. **B** Newey-West Standard Errors. Group-level maps show the spatial distribution of standard error estimates, account for within-individual variability and between-individual variability (see Group-level Analysis). Smaller values indicate greater precision in the timescale estimates within and between subjects. **C** T-Statistics. Maps display unthresholded and uncorrected t-ratios (see (66)), testing whether timescale at each surface coordinate exceed a half second. **D** Relative Standard Errors (RSEs). Maps show the relative reliability of timescale estimates across brain regions and subjects. Low RSE indicates high precision with small uncertainty, while high RSE suggests lower reliability of the estimates. **E** The T1w/T2w ratio from the Human Connectome Project maps cortical myelination, included here as a visual comparator to the spatial organization of timescales. This ratio is a useful proxy for mapping the sensory-associative axis of the brain, where sensory areas (e.g. primary visual and motor cortices; red) need fast signal transmission and high myelin levels, while associative regions (e.g. prefrontal cortex; blue) are less myelinated.

3.3 Estimation of rfMRI Timescale Maps

Subject-level timescale maps were derived from the Human Connectome Project dataset by independently fitting both LLS and NLS estimators to each cortical surface coordinate, using a mass-univariate approach to produce subject-level maps of timescale estimates and their associated standard errors. This method allows for spatially resolved estimates across the brain’s cortical surface, enabling a detailed comparison of the two estimated timescale maps. **Panel A** presents the spatial distribution of timescale estimates, revealing that, consistent with the simulation results, NLS estimates tend to yield larger timescales than LLS. **Panel B** shows the corresponding maps of standard errors, which appear spatially correlated with the timescale estimates, consistent with the simulation finding that larger timescales are associated with greater sampling variability. **Panel C** depicts the relative ratio of timescale estimates to their standard errors (i.e., t-statistics), testing whether the timescales significantly exceed a half second ($H_0 : \tau \leq 1$). Despite the larger standard errors for higher timescales,

these regions exhibit higher t-statistics, particularly for the NLS estimator, where t-statistics extend further into the tail of the distribution, indicating stronger evidence against the null hypothesis. This result is in line with simulations, which demonstrated that NLS provides higher signal-to-noise ratios for very large timescales compared to LLS. **Panel D** shows low RSEs across much of the brain indicating high estimation reliability. Overall, the LLS and NLS methods show comparable spatial organization of timescales across the cortical surface, but they diverge at the extremes—NLS tends to estimate much larger timescales, while LLS is more reliable for very small timescales, consistent with their differing behavior in boundary cases observed in the simulations.

Group-level timescale maps were generated by combining individual estimates to account for both within-individual and between-individual variability, providing an aggregate view of timescale distributions across subjects. **Panel A** shows that the average timescale maps for both LLS and NLS estimators are smoother than the individual maps, displaying a well-organized spatial pattern across the cortex, with NLS estimates generally being larger than LLS. **Panel B** presents the standard error maps, which combine variances from within-subject Newey-West estimates and between-subject timescale estimates. As expected, the standard errors are larger for NLS than for LLS. **Panel C** depicts t-statistics testing whether timescales exceed a half second, showing that while both methods yield comparable results, NLS produces more extreme t-statistics. **Panel D** plots relative standard errors (RSEs), illustrating the general trend that regions with larger timescales are easier to estimate, while areas with smaller timescales exhibit greater uncertainty. Overall, these group-level maps highlight consistent spatial organization of timescales maps of the cortical surface. **Panel E** this organizing pattern has been compared in previous studies to the myelination gradient (T1w/T2w ratio), which aligns with the sensory-associative axis of brain function. At a very coarse approximation, this map appears weakly correlated with the timescale maps, where timescales increase from sensory to associative regions.

4 Discussion

This study addresses gaps in current methodology for estimating neural timescales by introducing robust statistical techniques for mapping timescales across brain regions. Providing a detailed account of the large-sample properties of the two most commonly applied timescale estimators – the time-domain linear model and the autocorrelation-domain nonlinear model – we show that both behave consistently under broad assumptions of stationarity and ergodicity. Importantly, we demonstrate that the standard errors of both estimators are also consistent under the same general conditions, enabling statistical inference and hypothesis testing. This advancement addresses a notable limitation in most neural timescale studies, which often report only point estimates without appropriate measures of uncertainty, thereby limiting inference and testing.

Through parameter recovery simulations, we demonstrate that both models yield valid timescale estimates along with corresponding standard errors as a way to assess precision of estimation. Comparing the two, the time-domain linear model 2.2.1 offers greater computational efficiency and estimation stability for small timescales. In contrast, the autocorrelation-domain nonlinear model 2.2.2 provides greater estimation stability for large timescales, i.e., when long-range temporal dependencies are present. Across both models, the introduction of Newey-West corrected standard errors mitigates the downward bias in the standard error estimators under a broad range of time processes, enhancing the reliability of inference and testing [27]. This is shown in AR(2) and empirical resting fMRI (rfMRI) simulations, where the fitted models are misspecified relative to the data-generating process. Lastly, when applied to rfMRI data from the Human Connectome Project, both methods produce timescale and t-statistic maps that appear consistent with previously reported anatomical hierarchies in the brain [38]. Timescale cortical maps from a range of other studies converge with the present rfMRI results to show that timescales are larger in associative versus sensory processing cor-

tices [29, 34, 18, 23, 15, 41, 35, 20, 14, 26]. This provides some assurance that the methods described here are measuring biologically interpretable parameters about the "memory" or "persistence" of neural processes. That said, the interpretation of timescale maps is beyond the scope of the present paper and a topic for future research.

This segues to potential limitations in our approach. Although the use of rfMRI offers dense spatial sampling relative to other imaging modalities (EEG, MEG, ECoG), its sparse temporal sampling may introduce bias and variance in estimation. The estimator properties we discussed (consistency and limiting variance) depend on large-sample asymptotics. In practice, we use finite samples, and when the underlying hemodynamic process is sampled at a low frequency and exhibits strong temporal dependence, the effective sample size may be too small [1, 15]. Furthermore, the non-specific metabolic and neuronal origins of the hemodynamic signal make mechanistic timescale interpretations difficult [29, 11]. On the methodological side, while our models handle misspecification to some extent, cases remain where the underlying process may deviate from the assumptions of stationarity and ergodicity, impacting the reliability of timescale estimates [9, chapter 14.7]. Extending model definitions to account for nonstationarity, where autocorrelations are time-dependent, might provide more accurate maps, especially in task-based or dynamic fMRI paradigms [11]. Additionally, adding standard errors to the frequency-domain approach to timescale estimation would allow for the direct modeling of oscillations, which is important when working with electrophysiological recordings of the brain [4, 6].

In conclusion, this paper introduces robust estimators for timescales and their standard errors in rfMRI, enabling more rigorous statistical comparisons across brain regions, experimental conditions, and subjects. This advances the field toward more reliable and interpretable neural timescale maps. The methods presented here for mapping the spatial organization of timescales allow for inference and testing by moving beyond point estimates to incorporate variability. The work lays the methodological foundation for future research on the role of timescales in brain structure and function.

5 Code and Data Availability

All simulation results and fMRI timescale maps, inclusive of the code by which they were derived, can be accessed on GitHub/fmri-timescales. The code is under the open-source MIT license, permitting access and reuse with attribution. The Human Connectome Project's young adult dataset (ages 22-35; 2018 release) used in this study is publicly accessible under a data usage agreement, which outlines specific terms for data usage and sharing.

References

- [1] S. Afyouni, S. M. Smith, and T. E. Nichols. Effective degrees of freedom of the Pearson's correlation coefficient under autocorrelation. *NeuroImage*, 199:609–625, Oct. 2019. ISSN 10538119. doi: 10.1016/j.neuroimage.2019.05.011. URL <https://linkinghub.elsevier.com/retrieve/pii/S1053811919303945>.
- [2] G. Buzsáki. Large-scale recording of neuronal ensembles. *Nature Neuroscience*, 7(5):446–451, May 2004. ISSN 1097-6256, 1546-1726. doi: 10.1038/nn1233. URL <https://www.nature.com/articles/nn1233>.
- [3] R. Cirillo, V. Fascianelli, L. Ferrucci, and A. Genovesio. Neural Intrinsic Timescales in the Macaque Dorsal Premotor Cortex Predict the Strength of Spatial Response Coding. *iScience*, 10:203–210, Dec. 2018. ISSN 25890042. doi: 10.1016/j.isci.2018.11.033. URL <https://linkinghub.elsevier.com/retrieve/pii/S2589004218302232>.

- [4] T. Donoghue, M. Haller, E. J. Peterson, P. Varma, P. Sebastian, R. Gao, T. Noto, A. H. Lara, J. D. Wallis, R. T. Knight, A. Shestyuk, and B. Voytek. Parameterizing neural power spectra into periodic and aperiodic components. *Nature Neuroscience*, 23(12):1655–1665, Dec. 2020. ISSN 1097-6256, 1546-1726. doi: 10.1038/s41593-020-00744-x. URL <https://www.nature.com/articles/s41593-020-00744-x>.
- [5] J. Fallon, P. G. D. Ward, L. Parkes, S. Oldham, A. Arnatkevičiūtė, A. Fornito, and B. D. Fulcher. Timescales of spontaneous fMRI fluctuations relate to structural connectivity in the brain. *Network Neuroscience*, 4(3):788–806, Jan. 2020. ISSN 2472-1751. doi: 10.1162/netn_a_00151. URL <https://direct.mit.edu/netn/article/4/3/788-806/95846>.
- [6] R. Gao, R. L. van den Brink, T. Pfeffer, and B. Voytek. Neuronal timescales are functionally dynamic and shaped by cortical microarchitecture. *eLife*, 9:e61277, Nov. 2020. ISSN 2050-084X. doi: 10.7554/eLife.61277. URL <https://elifesciences.org/articles/61277>.
- [7] M. F. Glasser, S. N. Sotiropoulos, J. A. Wilson, T. S. Coalson, B. Fischl, J. L. Andersson, J. Xu, S. Jbabdi, M. Webster, J. R. Polimeni, D. C. Van Essen, and M. Jenkinson. The minimal pre-processing pipelines for the Human Connectome Project. *NeuroImage*, 80:105–124, Oct. 2013. ISSN 10538119. doi: 10.1016/j.neuroimage.2013.04.127. URL <https://linkinghub.elsevier.com/retrieve/pii/S1053811913005053>.
- [8] M. Golesorkhi, J. Gomez-Pilar, S. Tumati, M. Fraser, and G. Northoff. Temporal hierarchy of intrinsic neural timescales converges with spatial core-periphery organization. *Communications Biology*, 4(1):277, Mar. 2021. ISSN 2399-3642. doi: 10.1038/s42003-021-01785-z. URL <https://www.nature.com/articles/s42003-021-01785-z>.
- [9] B. E. Hansen. *Econometrics*. Princeton University Press, Princeton, 2022. ISBN 978-0-691-23589-9.
- [10] U. Hasson, E. Yang, I. Vallines, D. J. Heeger, and N. Rubin. A Hierarchy of Temporal Receptive Windows in Human Cortex. *The Journal of Neuroscience*, 28(10):2539–2550, Mar. 2008. ISSN 0270-6474, 1529-2401. doi: 10.1523/JNEUROSCI.5487-07.2008. URL <https://www.jneurosci.org/lookup/doi/10.1523/JNEUROSCI.5487-07.2008>.
- [11] B. J. He. Scale-Free Properties of the Functional Magnetic Resonance Imaging Signal during Rest and Task. *The Journal of Neuroscience*, 31(39):13786–13795, Sept. 2011. ISSN 0270-6474, 1529-2401. doi: 10.1523/JNEUROSCI.2111-11.2011. URL <https://www.jneurosci.org/lookup/doi/10.1523/JNEUROSCI.2111-11.2011>.
- [12] B. J. He, J. M. Zempel, A. Z. Snyder, and M. E. Raichle. The Temporal Structures and Functional Significance of Scale-free Brain Activity. *Neuron*, 66(3):353–369, May 2010. ISSN 08966273. doi: 10.1016/j.neuron.2010.04.020. URL <https://linkinghub.elsevier.com/retrieve/pii/S0896627310002916>.
- [13] Z. Huang, X. Liu, G. A. Mashour, and A. G. Hudetz. Timescales of Intrinsic BOLD Signal Dynamics and Functional Connectivity in Pharmacologic and Neuropathologic States of Unconsciousness. *The Journal of Neuroscience*, 38(9):2304–2317, Feb. 2018. ISSN 0270-6474, 1529-2401. doi: 10.1523/JNEUROSCI.2545-17.2018. URL <https://www.jneurosci.org/lookup/doi/10.1523/JNEUROSCI.2545-17.2018>.
- [14] T. Ito, L. J. Hearne, and M. W. Cole. A cortical hierarchy of localized and distributed processes revealed via dissociation of task activations, connectivity changes, and intrinsic timescales. *NeuroImage*, 221:117141, Nov. 2020. ISSN 10538119. doi: 10.1016/j.neuroimage.2020.117141. URL <https://linkinghub.elsevier.com/retrieve/pii/S1053811920306273>.

- [15] Y. Kaneoke, T. Donishi, J. Iwatani, S. Ukai, K. Shinosaki, and M. Terada. Variance and Autocorrelation of the Spontaneous Slow Brain Activity. *PLoS ONE*, 7(5):e38131, May 2012. ISSN 1932-6203. doi: 10.1371/journal.pone.0038131. URL <https://dx.plos.org/10.1371/journal.pone.0038131>.
- [16] S. Li and X.-J. Wang. Hierarchical timescales in the neocortex: Mathematical mechanism and biological insights. *Proceedings of the National Academy of Sciences*, 119(6):e2110274119, Feb. 2022. ISSN 0027-8424, 1091-6490. doi: 10.1073/pnas.2110274119. URL <https://pnas.org/doi/full/10.1073/pnas.2110274119>.
- [17] N. K. Logothetis. What we can do and what we cannot do with fMRI. *Nature*, 453(7197):869–878, June 2008. ISSN 0028-0836, 1476-4687. doi: 10.1038/nature06976. URL <https://www.nature.com/articles/nature06976>.
- [18] D. J. Lurie, I. Pappas, and M. D’Esposito. Cortical timescales and the modular organization of structural and functional brain networks. *Human Brain Mapping*, 45(2):e26587, Feb. 2024. ISSN 1065-9471, 1097-0193. doi: 10.1002/hbm.26587. URL <https://onlinelibrary.wiley.com/doi/10.1002/hbm.26587>.
- [19] D. J.-N. Maisson, T. V. Cash-Padgett, M. Z. Wang, B. Y. Hayden, S. R. Heilbronner, and J. Zimmermann. Choice-relevant information transformation along a ventrodorsal axis in the medial prefrontal cortex. *Nature Communications*, 12(1):4830, Aug. 2021. ISSN 2041-1723. doi: 10.1038/s41467-021-25219-w. URL <https://www.nature.com/articles/s41467-021-25219-w>.
- [20] A. M. Manea, A. Zilverstand, K. Ugurbil, S. R. Heilbronner, and J. Zimmermann. Intrinsic timescales as an organizational principle of neural processing across the whole rhesus macaque brain. *eLife*, 11:e75540, Mar. 2022. ISSN 2050-084X. doi: 10.7554/eLife.75540. URL <https://elifesciences.org/articles/75540>.
- [21] A. M. G. Manea, D. J.-N. Maisson, B. Voloh, A. Zilverstand, B. Hayden, and J. Zimmermann. Neural timescales reflect behavioral demands in freely moving rhesus macaques. *Nature Communications*, 15(1):2151, Mar. 2024. ISSN 2041-1723. doi: 10.1038/s41467-024-46488-1. URL <https://www.nature.com/articles/s41467-024-46488-1>.
- [22] C. Meisel, K. Bailey, P. Achermann, and D. Plenz. Decline of long-range temporal correlations in the human brain during sustained wakefulness. *Scientific Reports*, 7(1):11825, Sept. 2017. ISSN 2045-2322. doi: 10.1038/s41598-017-12140-w. URL <https://www.nature.com/articles/s41598-017-12140-w>.
- [23] A. Mitra, A. Z. Snyder, C. D. Hacker, and M. E. Raichle. Lag structure in resting-state fMRI. *Journal of Neurophysiology*, 111(11):2374–2391, June 2014. ISSN 0022-3077, 1522-1598. doi: 10.1152/jn.00804.2013. URL <https://www.physiology.org/doi/10.1152/jn.00804.2013>.
- [24] S. Moeller, E. Yacoub, C. A. Olman, E. Auerbach, J. Strupp, N. Harel, and K. Uğurbil. Multiband multislice GE-EPI at 7 tesla, with 16-fold acceleration using partial parallel imaging with application to high spatial and temporal whole-brain fMRI. *Magnetic Resonance in Medicine*, 63(5):1144–1153, 2010. ISSN 1522-2594. doi: 10.1002/mrm.22361. URL <https://onlinelibrary.wiley.com/doi/abs/10.1002/mrm.22361>. _eprint: <https://onlinelibrary.wiley.com/doi/pdf/10.1002/mrm.22361>.
- [25] J. D. Murray, A. Bernacchia, D. J. Freedman, R. Romo, J. D. Wallis, X. Cai, C. Padoa-Schioppa, T. Pasternak, H. Seo, D. Lee, and X.-J. Wang. A hierarchy of intrinsic timescales across primate cortex. *Nature Neuroscience*, 17(12):1661–1663, Dec. 2014. ISSN 1097-6256, 1546-1726. doi: 10.1038/nn.3862. URL <http://www.nature.com/articles/nn.3862>.
- [26] E. J. Müller, B. Munn, L. J. Hearne, J. B. Smith, B. Fulcher, A. Arnatkevičiūtė, D. J. Lurie, L. Cocchi, and J. M. Shine. Core and matrix thalamic sub-populations relate to spatio-temporal cortical connectivity gradients. *NeuroImage*, 222:117224, Nov. 2020. ISSN 10538119. doi: 10.1016/j.neuroimage.2020.117224. URL <https://linkinghub.elsevier.com/retrieve/pii/S1053811920307102>.

- [27] W. Newey and K. West. A simple, positive semi-definite, heteroskedasticity and autocorrelation-consistent covariance matrix. *Econometrica*, 55(3):703–08, 1987.
- [28] S. Nougaret, V. Fascianelli, S. Ravel, and A. Genovesio. Intrinsic timescales across the basal ganglia. *Scientific Reports*, 11(1):21395, Nov. 2021. ISSN 2045-2322. doi: 10.1038/s41598-021-00512-2. URL <https://www.nature.com/articles/s41598-021-00512-2>.
- [29] R. V. Raut, A. Z. Snyder, and M. E. Raichle. Hierarchical dynamics as a macroscopic organizing principle of the human brain. *Proceedings of the National Academy of Sciences*, 117(34):20890–20897, Aug. 2020. ISSN 0027-8424, 1091-6490. doi: 10.1073/pnas.2003383117. URL <https://pnas.org/doi/full/10.1073/pnas.2003383117>.
- [30] E. C. Robinson, S. Jbabdi, M. F. Glasser, J. Andersson, G. C. Burgess, M. P. Harms, S. M. Smith, D. C. Van Essen, and M. Jenkinson. MSM: A new flexible framework for Multimodal Surface Matching. *NeuroImage*, 100:414–426, Oct. 2014. ISSN 10538119. doi: 10.1016/j.neuroimage.2014.05.069. URL <https://linkinghub.elsevier.com/retrieve/pii/S1053811914004546>.
- [31] R. Rossi-Pool, A. Zainos, M. Alvarez, S. Parra, J. Zizumbo, and R. Romo. Invariant timescale hierarchy across the cortical somatosensory network. *Proceedings of the National Academy of Sciences*, 118(3):e2021843118, Jan. 2021. ISSN 0027-8424, 1091-6490. doi: 10.1073/pnas.2021843118. URL <https://pnas.org/doi/10.1073/pnas.2021843118>.
- [32] C. A. Runyan, E. Piasini, S. Panzeri, and C. D. Harvey. Distinct timescales of population coding across cortex. *Nature*, 548(7665):92–96, Aug. 2017. ISSN 0028-0836, 1476-4687. doi: 10.1038/nature23020. URL <https://www.nature.com/articles/nature23020>.
- [33] G. Salimi-Khorshidi, G. Douaud, C. F. Beckmann, M. F. Glasser, L. Griffanti, and S. M. Smith. Automatic denoising of functional MRI data: Combining independent component analysis and hierarchical fusion of classifiers. *NeuroImage*, 90:449–468, Apr. 2014. ISSN 10538119. doi: 10.1016/j.neuroimage.2013.11.046. URL <https://linkinghub.elsevier.com/retrieve/pii/S1053811913011956>.
- [34] G. Shafiei, R. D. Markello, R. Vos De Wael, B. C. Bernhardt, B. D. Fulcher, and B. Misic. Topographic gradients of intrinsic dynamics across neocortex. *eLife*, 9:e62116, Dec. 2020. ISSN 2050-084X. doi: 10.7554/eLife.62116. URL <https://elifesciences.org/articles/62116>.
- [35] M. Shinn, A. Hu, L. Turner, S. Noble, K. H. Preller, J. L. Ji, F. Moujaes, S. Achard, D. Scheinost, R. T. Constable, J. H. Krystal, F. X. Vollenweider, D. Lee, A. Anticevic, E. T. Bullmore, and J. D. Murray. Functional brain networks reflect spatial and temporal autocorrelation. *Nature Neuroscience*, pages 1–12, Apr. 2023. ISSN 1546-1726. doi: 10.1038/s41593-023-01299-3. URL <https://www.nature.com/articles/s41593-023-01299-3>. Publisher: Nature Publishing Group.
- [36] S. M. Smith, J. Andersson, E. J. Auerbach, C. F. Beckmann, J. Bijsterbosch, G. Douaud, E. Duff, D. A. Feinberg, L. Griffanti, M. P. Harms, M. Kelly, T. Laumann, K. L. Miller, S. Moeller, S. Petersen, J. Power, G. Salimi-Khorshidi, A. Z. Snyder, A. Vu, M. W. Woolrich, J. Xu, E. Yacoub, K. Ugurbil, D. Van Essen, and M. F. Glasser. Resting-state fMRI in the Human Connectome Project. *NeuroImage*, 80:144–168, Oct. 2013. ISSN 1053-8119. doi: 10.1016/j.neuroimage.2013.05.039. URL <https://www.ncbi.nlm.nih.gov/pmc/articles/PMC3720828/>.
- [37] G. J. Stephens, C. J. Honey, and U. Hasson. A place for time: the spatiotemporal structure of neural dynamics during natural audition. *Journal of Neurophysiology*, 110(9):2019–2026, Nov. 2013. ISSN 0022-3077, 1522-1598. doi: 10.1152/jn.00268.2013. URL <https://www.physiology.org/doi/10.1152/jn.00268.2013>.

- [38] D. C. Van Essen, S. M. Smith, D. M. Barch, T. E. Behrens, E. Yacoub, and K. Ugurbil. The WU-Minn Human Connectome Project: An overview. *NeuroImage*, 80:62–79, Oct. 2013. ISSN 10538119. doi: 10.1016/j.neuroimage.2013.05.041. URL <https://linkinghub.elsevier.com/retrieve/pii/S1053811913005351>.
- [39] D. F. Wasmuht, E. Spaak, T. J. Buschman, E. K. Miller, and M. G. Stokes. Intrinsic neuronal dynamics predict distinct functional roles during working memory. *Nature Communications*, 9(1):3499, Aug. 2018. ISSN 2041-1723. doi: 10.1038/s41467-018-05961-4. URL <https://www.nature.com/articles/s41467-018-05961-4>.
- [40] T. Watanabe, G. Rees, and N. Masuda. Atypical intrinsic neural timescale in autism. *eLife*, 8: e42256, Feb. 2019. ISSN 2050-084X. doi: 10.7554/eLife.42256. URL <https://elifesciences.org/articles/42256>.
- [41] K. Wengler, A. T. Goldberg, G. Chahine, and G. Horga. Distinct hierarchical alterations of intrinsic neural timescales account for different manifestations of psychosis. *eLife*, 9:e56151, Oct. 2020. ISSN 2050-084X. doi: 10.7554/eLife.56151. URL <https://elifesciences.org/articles/56151>.
- [42] R. Zeraati, T. A. Engel, and A. Levina. A flexible Bayesian framework for unbiased estimation of timescales. *Nature Computational Science*, 2(3):193–204, Mar. 2022. ISSN 2662-8457. doi: 10.1038/s43588-022-00214-3. URL <https://www.nature.com/articles/s43588-022-00214-3>.
- [43] F. Zilio, J. Gomez-Pilar, S. Cao, J. Zhang, D. Zang, Z. Qi, J. Tan, T. Hiromi, X. Wu, S. Fogel, Z. Huang, M. R. Hohmann, T. Fomina, M. Synofzik, M. Grosse-Wentrup, A. M. Owen, and G. Northoff. Are intrinsic neural timescales related to sensory processing? Evidence from abnormal behavioral states. *NeuroImage*, 226:117579, Feb. 2021. ISSN 10538119. doi: 10.1016/j.neuroimage.2020.117579. URL <https://linkinghub.elsevier.com/retrieve/pii/S1053811920310648>.